

Efficiencies of Magnetic-Field Amplification and Electron Acceleration in Young Supernova Remnants: Global Averages and Kepler’s Supernova Remnant

STEPHEN P. REYNOLDS,¹ BRIAN J. WILLIAMS,² KAZIMIERZ J. BORKOWSKI,³ AND KNOX S. LONG⁴

¹*Department of Physics, North Carolina State University,
Raleigh, NC 27695-8202*

²*NASA/GSFC, Code 660, Greenbelt, MD 20771*

³*Department of Physics, North Carolina State University, Raleigh, NC 27695-8202*

⁴*Space Telescope Science Institute, 3700 San Martin Drive, Baltimore, MD, 21218*

ABSTRACT

Particle acceleration to suprathermal energies in strong astrophysical shock waves is a widespread phenomenon, generally explained by diffusive shock acceleration. Such shocks can also amplify upstream magnetic field considerably beyond simple compression. The complex plasma physics processes involved are often parameterized by assuming that shocks put some fraction ϵ_e of their energy into fast particles, and another fraction ϵ_B into magnetic field. Modelers of shocks in supernovae, supernova remnants, and gamma-ray bursters, among other locations, often assume typical values for these fractions, presumed to remain constant in time. However, it is rare that enough properties of a source are independently constrained that values of the epsilons can be inferred directly. Supernova remnants (SNRs) can provide such circumstances. Here we summarize results from global fits to spatially integrated emission in six young SNRs, finding $10^{-4} \lesssim \epsilon_e \lesssim 0.05$ and $0.001 \lesssim \epsilon_B \lesssim 0.1$. These large variations might be put down to the differing ages and environments of these SNRs, so we conduct a detailed analysis of a single remnant, that of Kepler’s supernova. Both epsilons can be determined at seven different locations around the shock, and we find even larger ranges for both epsilons, as well as for their ratio (thus independent of the shock energy itself). We conclude that unknown factors have a large influence on the efficiency of both processes. Shock obliquity, upstream neutral fraction, or other possibilities need to be explored, while calculations assuming fixed values of the epsilons should be regarded as provisional.

1. INTRODUCTION

Strong shocks in supernovae, supernova remnants (SNRs), and gamma-ray bursters (GRB sources) are widely observed to produce nonthermal particle distributions and to amplify ambient magnetic fields (e.g., Weiler et al. 2002; Reynolds et al. 2008; van Paradijs et al. 2000). The total energy in these nonthermal components is generally small compared to bulk thermal and kinetic energies; to produce the Galactic cosmic rays, roughly 10% of supernova energy is adequate. The processes responsible for particle acceleration and magnetic-field amplification are fairly well understood in broad terms (see any of various reviews, such as Blandford & Eichler 1987; Malkov & Drury 2001; Ressler et al. 2014) but details remain frustratingly elusive. Even as basic an issue as the fraction of shock energy eventually winding up in particles and magnetic field is difficult to predict from first principles, and may evolve with changing conditions.

Observational constraints on these quantities are also surprisingly hard to come by. An early attempt at using the spatial structure of radio images of young supernova remnants (SNRs) to discriminate among models for magnetic-field evolution (Reynolds & Chevalier 1981) compared theoretical profiles of SNR radio emission assuming uniform post-shock magnetic-field strength (shock expanding into constant magnetic field, with only compression increasing the post-shock value), with a model with magnetic energy density u_B amplified to a value proportional to post-shock pressure P_2 . (The post-shock pressure in a strong shock from the Rankine-Hugoniot jump conditions is $P_2 = [2/(\gamma + 1)]\rho_0 v_s^2$ or $3\rho_0 v_s^2/4$ for adiabatic index $\gamma = 5/3$, where ρ_0 is the upstream gas density and v_s the shock speed. P_2 is also proportional to the total thermal energy density e_2 : $e_2 = P_2/(\gamma - 1)$, so that $\rho_0 v_s^2 = [(\gamma + 1)(\gamma - 1)/2]e_2 = (8/9)e_2$ for $\gamma = 5/3$. The convention has been to absorb the factor 8/9 into the definitions of the ϵ efficiency factors, and we shall follow that convention here: $\epsilon_e \equiv u_e/\rho_0 v_s^2$ and $\epsilon_B \equiv (B^2/8\pi)/\rho_0 v_s^2$.)

Reynolds & Chevalier (1981) found substantial differences between predictions of their two models for magnetic field: amplified-field models predicted that the radio profile should rise from the shock inward all the way to the contact discontinuity between shocked ejecta and shocked ambient material. However, various confounding effects made this prediction difficult to test. A similar test (Chomiuk & Wilcots 2009) used collective luminosity functions of extragalactic SNRs to try to discriminate between these models, finding that (assuming a constant cosmic-ray energy density) the swept-up model was less favored by the data. However, the assumption of a non-evolving relativistic-electron density is not supported by more recent studies of diffusive shock acceleration (DSA). See, for instance, Riquelme & Spitkovsky (2011).

The dependence of the synchrotron luminosity on both the energy density of relativistic electrons and of magnetic field plagues attempts to use synchrotron emission as a diagnostic in contexts as disparate as active galactic nuclei, gamma-ray burst sources, the interstellar medium of normal galaxies, supernovae, nova and supernova remnants, pulsar-wind nebulae, and elsewhere. By now the assumption of equipartition of energy between particles and field has been largely abandoned. Originally introduced to obtain a lower limit to the energy required to explain extended emission in radio galaxies (in particular M87; Burbidge 1956), the assumption took on a life of its own, supported by no more than a vague sense that Nature ought to put equal amounts of energy in each available form. The difficulty of deciding how much energy might reside in relativistic protons has meant that apart from providing absolute lower limits for energy arguments, in which case one ignores energy in protons, the assumption has substantial model dependence, and its utility and predictive power are limited.

The assumption of constant fractions of shock energy going into relativistic electrons (ϵ_e) and magnetic field (ϵ_B) is implicit in Reynolds & Chevalier (1981), and made explicitly in Chevalier (1984). It appears to have been the standard assumption in early GRB modeling, which seems to be where the ϵ notation originated (e.g., Sari et al. 1998). The notation, and the assumption that these fractions remain constant as the shock wave evolves, have become widespread in modeling radio emission from supernovae and SNRs as well as GRBs (e.g., Lundqvist et al. 2020). Typical assumed values for these fractions are in the range 0.01 to 0.1 for GRBs (e.g., Nava et al. 2014). However, Panaitescu & Kumar (2001) fit a multiparameter model for GRB afterglows to 8 events, finding values ranging over an order of magnitude for ϵ_e ($10^{-2} - 10^{-1}$) and three orders of magnitude for ϵ_B ($10^{-4} - 10^{-1}$). In general, both the values and the assumption of constancy lack the observational support one would like in such fundamental quantities. Additionally, the relativistic shocks inferred in GRB afterglows may have qualitatively different effects in both magnetic-field amplification and electron acceleration than would be found in nonrelativistic shocks in SNRs. Numerical simulations (e.g., Crumley et al. 2019) show substantial shock-velocity dependence in ϵ_e , as well as dependence on other shock parameters. In SNR studies, more recent work has attempted to simulate the acceleration of electrons and amplification of magnetic field based on analytic prescriptions, so that the values of ϵ_e and ϵ_B can evolve (e.g., Sarbadhicary et al. 2017; Pavlović et al. 2018). However, these studies also assume parameters such as a fixed ratio of cosmic-ray electron to ion energy, or a fixed injection efficiency into the acceleration process, that affect the behavior of the ϵ factors.

It is the goal of this paper to determine as well as possible the values of ϵ_e and ϵ_B in young supernova remnants, using the best observational data available, and making minimal theoretical assumptions. We discuss methods for determining magnetic-field strengths in Section 2, and for extracting relativistic-electron energy densities in Section 3. We then apply these to estimate average ϵ factors for several young SNRs, in Section 4. The core of the paper is in Sections 5 and 6, where we obtain spatially resolved values of the ϵ factors at seven locations around the rim of Kepler’s SNR. The results are discussed in Section 7 and summarized in Section 8.

2. MAGNETIC-FIELD DETERMINATIONS

There are various methods for obtaining independent measures of magnetic field in compact synchrotron sources. One interesting method, applicable to radio supernovae, produces some valuable information on the values and evolution of u_B and ϵ_B , so shall be described here. While this method cannot be applied to SNRs, it does allow inferences of those quantities over time as a supernova evolves. The unsettling results (at least for SN 1993J) set the stage for our considerations of SNRs.

2.1. Synchrotron self-absorption in supernovae

This method, applicable whenever the process operates, relies on synchrotron self-absorption (SSA): the observation of the frequency at which a source becomes optically thin to synchrotron radiation, and the flux at that frequency, allow the determination of two out of the three quantities: source size, magnetic field, and electron energy density. However, the operation of SSA at observable radio frequencies requires conditions in a diffuse source that are fairly restrictive. Using the notation of Pacholczyk (1970), the absorption coefficient for a homogeneous synchrotron source with magnetic field B and electron energy spectrum KE^{-s} can be written

$$\kappa_\nu = c_6(s) (1.25 \times 10^{19})^{(s+4)/2} c_9(s+1) K B^{(s+2)/2} \nu^{-(s+4)/2} \text{ cm}^{-1} \quad (1)$$

where the numerical constants are given in Pacholczyk (1970). For a typical electron energy index $s = 2.5$ (synchrotron spectral index $\alpha \equiv (s - 1)/2 = 0.75$, with $S_\nu \propto \nu^{-\alpha}$), this is

$$\kappa_\nu = 6.13 \times 10^{21} K B^{9/4} \nu^{-13/4} \text{ cm}^{-1}. \quad (2)$$

If $s > 2$, the energy density in electrons u_e depends only on the lower energy limit to the spectrum E_l . Synchrotron emission basically requires $E_l \gtrsim 10m_e c^2$. An estimate of the required conditions for observable synchrotron self-absorption can be made by characterizing both K and B in terms of energy densities. If u_e and u_B are both equal to some nonthermal energy density u_{nonth} , then a source of line-of-sight extent L will become opaque to SSA below a frequency of about

$$\nu_1 \sim 2 \times 10^6 L^{4/13} u_{\text{nonth}}^{17/26} \text{ Hz} \quad (3)$$

(still for $s = 2.5$), and for that frequency to exceed 100 MHz, the source extent must satisfy

$$L \gtrsim 3 \times 10^5 u_{\text{nonth}}^{-17/8} \text{ cm}. \quad (4)$$

For a source extent less than 1 pc, the nonthermal energy density must exceed about $10^{-6} \text{ erg cm}^{-3}$, or about 1 MeV cm^{-3} . Thus SSA is an important effect only for very high energy-density circumstances, such as supernovae – but not SNRs.

Most radio supernovae show evolving spectra with a peak at some frequency which moves lower with time, attributed to synchrotron emission with some opacity setting in at lower frequencies. Some combination of free-free absorption, either coincident or foreground, and SSA is likely responsible (e.g., Chevalier 1984; Weiler et al. 2002). An extensive study by Chevalier (1998) attributes low-frequency absorption in 8 of 13 radio supernovae to SSA. He reduces the three required source parameters to two by assuming a fixed ratio (not necessarily one) of u_e to u_B , and derives source sizes and magnetic fields on the assumption that $u_B \propto \rho v_s^2$, the post-shock pressure. Magnetic-field strengths depend fairly weakly on all parameters, and are in the range 0.1 – 0.6 G, at the time of the emission peak.

In one case, SN 1993J, the radio observations are sufficiently frequent and the frequency coverage so extensive as to allow a detailed determination of u_e and u_B independently and as a function of time (Fransson & Björnsson 1998), since the VLBI observations of a more-or-less constant expansion velocity (for the first ~ 100 days) of $2 \times 10^4 \text{ km s}^{-1}$ (Bartel et al. 1994) allow the radius to be inferred. They find that $u_e \propto \rho v_s^2$ describes the data well, and much better than $u_e \propto \rho$ alone (here ρ is the upstream, i.e., circumstellar-medium [CSM], density). They determine $\epsilon_e \sim 5 \times 10^{-4}$. For magnetic field, the apparent deceleration beginning around day 100, with $R \propto t^m$ and $m = 0.74$, allows a discrimination between a model with $u_B \propto \rho v_s^2$ and one with $B \propto 1/R$, with the latter description providing a better fit to data. Before Day 100, they find $u_B/\rho v_s^2 \sim 0.14$, independent of time. The suggestions of non-constant ϵ_B , and worse, of a change in the very dependence of ϵ_B on SN parameters, are worrisome hints that the simple picture of constant epsilons is a poor description of the processes of shock acceleration and magnetic-field amplification. While we can only observe SNRs evolve through a small fraction of their lifetimes, the results of SN 1993J should put us on notice that results for SNRs may fail to tell a complete picture.

The detailed SN inferences rely on a simple one-zone emission model (though with spectral sophistication; Fransson & Björnsson (1998) evolve the electron distribution under both Coulomb and synchrotron losses), and on the operation of SSA as an absorption mechanism. They also apply to very high shock velocities and dense CSM. The importance of the processes of magnetic-field amplification and particle acceleration is sufficiently great that testing assumptions such as the scaling of u_e and u_B with density and shock velocity, and possible evolution of efficiencies with time, in different regions of parameter space, is a high priority. It is fortunate that methods exist to allow this in SNRs, especially to replace SSA for magnetic-field determinations.

2.2. Magnetic-field determinations in supernova remnants

SNRs are far too diffuse for SSA to be an important mechanism, so inferences of magnetic-field strengths rely on different techniques. Reynolds et al. (2012a) review these. Of particular interest is the “thin rims” argument, based on observations of X-ray synchrotron emission from young SNRs (Bamba et al. 2003; Vink & Laming 2003; Parizot et al. 2006), in particular, on the commonly observed morphology of thin tangential rims at the shock front (located, for instance, by $H\alpha$ observations). This method relies on the assumption that the disappearance of emission a short distance downstream results from synchrotron losses on the emitting electrons as they are advected (or diffuse) downstream. A thorough treatment is given by Ressler et al. (2014), who also include a discussion of an alternative explanation for thin rims, decay of magnetic turbulence downstream (Pohl et al. 2005). Under the simplest assumptions (electron transport by pure advection, ignoring magnetic-field damping, the delta-function approximation for the single-electron emitted spectrum), a straightforward relation can be derived between rim

thickness and magnetic-field strength (Parizot et al. 2006):

$$B \cong 210 \left(\frac{v_s}{1000 \text{ km s}^{-1}} \right)^{2/3} \left(\frac{w}{0.01 \text{ pc}} \right)^{-2/3} \mu\text{G} \quad (5)$$

where w is the filament width in the radial direction. (We have assumed a small geometric correction factor $(4\bar{P}/r_{\text{comp}})$ to be unity, where r_{comp} is the compression ratio and $\bar{P} = 1$ for a perfect sphere. Since we will always be employing this relation in small regions at the very edge of the remnant, the locally spherical approximation should be quite good.) However, more elaborate treatments produce somewhat different values; Ressler et al. (2014) collect published values for the remnant SN 1006 ranging from 65 to 130 μG , with one report of 14 μG . All agree, however, in requiring amplification of magnetic field beyond simple shock compression. The situation is made more complicated by the presence in a few cases of thin radio rims, produced by electrons with energies far too low to be affected by synchrotron losses, and thus requiring magnetic damping, a process with few theoretical or observational constraints.

Given B , we then have the magnetic-field energy density $u_B \equiv B^2/8\pi$. We note that if B is determined in this way, a prediction results for $\epsilon_B \propto B^2/v_s^2 \propto v_s^{-2/3}$, other things being equal. We shall apply Equation 5 in the analysis below.

3. RELATIVISTIC-ELECTRON ENERGY DENSITIES

We shall use observations of radio synchrotron intensity to obtain relativistic-electron energy densities, assuming simple power-law electron energy distributions. We take $N(E) = KE^{-s}$ electrons $\text{cm}^{-3} \text{erg}^{-1}$. The electron energy density is then

$$u_e \equiv \int_{E_l}^{E_h} K E^{1-s} dE = \frac{K}{s-2} E_l^{2-s} \left[1 - \left(\frac{E_h}{E_l} \right)^{2-s} \right]. \quad (6)$$

The energy ranges are somewhat arbitrary; for true synchrotron emission, $E_l \sim 10m_e c^2$ is a reasonable estimate, while since we shall have $s > 2$ and $E_h \gg E_l$, u_e is essentially independent of the value of E_h . So we approximate

$$u_e = \frac{K}{s-2} E_l^{2-s}. \quad (7)$$

Our strategy for finding K and hence u_e will be to observe synchrotron intensities, which in the optically thin limit are just proportional to the synchrotron emissivity j_ν . The synchrotron emissivity can be written (again in the notation of Pacholczyk (1970))

$$j_\nu = c_5(2c_1)^\alpha K B^{(s+1)/2} \nu^{-\alpha} \text{ erg cm}^{-3} \text{ s}^{-1} \text{ Hz}^{-1} \text{ sr}^{-1}. \quad (8)$$

Here c_5 is a function of the electron index s : $c_5 \sim 10^{-24}$ cgs for $2 < s < 3$, and $c_1 \equiv 6.27 \times 10^{18}$ cgs. The constants can be conveniently lumped together as

$$c_j \equiv c_5(2c_1)^\alpha. \quad (9)$$

For $s = 2.42$, its value for Kepler, $c_j(2.42) \equiv c_5(2.42)(2c_1)^{0.71} = 3.69 \times 10^{-10}$ cgs. Then

$$K = c_j^{-1} B^{-(s+1)/2} \nu^\alpha j_\nu. \quad (10)$$

We neglect synchrotron self-absorption for SNRs, so the intensity on any line of sight is just given by $\int j_\nu dl$.

We can infer global average values of the emissivity by measuring the total remnant flux at frequency ν , S_ν . For spatially resolved measurements, we shall measure local values of I_ν and estimate (short) line-of-sight depths L so $j_\nu = \langle I \rangle / L$. For a homogeneous source of volume V_{em} at distance d , we can write (assuming isotropic synchrotron emission, that is, disordered magnetic field)

$$S_\nu = (4\pi j_\nu) \frac{V_{\text{em}}}{4\pi d^2}. \quad (11)$$

We will first apply this to obtain a mean u_e for a spherical remnant of radius R where we take the emitting volume to be $V_{\text{em}} = (1/r_{\text{comp}})4\pi R^3/3$, where r_{comp} is the shock compression ratio. So $j_\nu = d^2 S_\nu / V_{\text{em}}$. Finally, the electron energy density u_e is given by

$$u_e = [E_l^{2-s}/(s-2)] c_j^{-1} B^{-(s+1)/2} \nu^\alpha d^2 S_\nu (3r_{\text{comp}}/4\pi R^3). \quad (12)$$

All quantities on the right are observable with the exception of the assumed value of E_l of $10m_e c^2$.

For Kepler's SNR, we shall consider small regions at the very edge of the remnant, and shall assume that j_ν is constant along our (short) lines of sight L , so the intensity $I_\nu = j_\nu L$. Then we obtain an expression for the electron energy density u_e :

$$u_e = [c_j(s)(s-2)]^{-1} E_l^{2-s} I_\nu L^{-1} B^{-(s+1)/2} \nu^\alpha. \quad (13)$$

Finally, we obtain $\epsilon_e \equiv u_e/\rho_0 v_s^2$ in either case.

Table 1. Magnetic Field Strengths in Young Remnants

Object	P+06	VBK05	RP12		T+15
			Loss	Damp	
Cas A	210-230	500	520	115-260	
Kepler	170-180	200	250	80-135	
Tycho	200-230	300	310	85-150	50-400
SN 1006	57-90	140	130	64-65	40-200
RCW 86		100			

NOTE—Magnetic-field strengths are in μGauss . References: P+06, Parizot et al. (2006); VBK05, Völk et al. (2005); RP12, Rettig & Pohl (2012); T+15, Tran et al. (2015)

4. SPATIALLY INTEGRATED DETERMINATIONS

Here we present spatially-averaged determinations of u_e and u_B for several young remnants: G1.9+0.3 (age ~ 100 yr); Cas A (~ 350 yr); Kepler (417 yr); Tycho (449 yr); SN 1006 (1015 yr); and RCW 86 (1836 yr, if SN 185 CE; Williams et al. 2011). We collect observations from the literature. Table 1 lists magnetic-field determinations using variants of Eq. 5 for these objects. The large dispersion in values from different authors illustrates the assumption-dependence of the analysis. The most complete discussion, including many subtle effects, can be found in Ressler et al. (2014). Additional data required to infer the mean relativistic-electron density are given in Table 2. Averaging over the entire remnant is a crude application of the magnetic-field results that strictly apply only to the particular rims which were measured.

For the results in Table 2, we chose the magnetic-field values of Parizot et al. (2006), except for RCW 86 for which we used the value from Völk et al. (2005). The value for G1.9+0.3 was obtained from the width of a thin rim in the west edge of $1.8''$ measured from the 2011 image (Borkowski et al. 2013), and using $v_s = 14,000 \text{ km s}^{-1}$ and $d = 8.5 \text{ kpc}$ (Reynolds et al. 2008). The various values in Table 1 range over about a factor of 3-4 at most, introducing a possible range of an order of magnitude in the values of u_B , u_e/u_B , and ϵ_B in Table 2. Even with this large possible range, however, the spread in values of u_e/u_B (independent of pressure) and ϵ_B is far greater. Given the heterogeneous input data, we have not attempted to quantify uncertainties, but it is likely that those due to the magnetic field are the dominant contribution to the error budget. At any rate, it seems exceptionally unlikely that the large spread in quantities such as u_e/u_B could be due to measurement uncertainties.

5. SPATIALLY RESOLVED EFFICIENCIES IN KEPLER’S SUPERNOVA REMNANT

The surprisingly large range of values of the various efficiency parameters listed in Table 2 applies across rather different SNRs, of different ages and properties. The environments of these SNRs are likely very different as well; one might hope to attribute the results of Table 2 to this heterogeneity. However, it is possible to use similar methods to analyze the conditions at different locations around the rim of a single remnant. This technique has obvious benefits in removing dependence on many quantities that vary between remnants, chiefly but not exclusively distance. Here we describe a spatially resolved analysis of the efficiencies of electron acceleration and magnetic-field amplification at different locations around the periphery of Kepler’s supernova remnant (“Kepler” hereafter). The distance to Kepler is uncertain, with values ranging from 4 kpc (Sankrit et al. 2005) to 8 kpc (e.g., Millard et al. 2019). Recent optical determinations suggest 5 kpc (Sankrit et al. 2016), and we shall assume 5 kpc here. However, the main import of our results will be in comparing inferences at different points, hence independent of distance.

5.1. Observational strategy

To fix the efficiencies of shock-energy deposition into magnetic field and relativistic electrons, one requires independent local measurements of density, shock velocity, magnetic-field strength, and electron energy density. Such measurements have substantial uncertainties for a SNR. X-ray diagnostics of plasma density are fraught with uncertainties, requiring spectral modeling and assumptions about filling factors. Shock velocity determinations from X-ray spectra suffer from uncertainty about prompt electron heating in the shock. These difficulties require alternative methods for determining each quantity.

An excellent diagnostic for the density of a hot plasma is the temperature of grains embedded in it (e.g., Dwek & Arendt 1992), which are collisionally heated by the plasma. We have previously employed this method to obtain post-shock densities of SNRs

Table 2. Derived Properties of Remnants

Remnant	B (μG)	S_9 (Jy)	d (kpc)	α^a	R (arcsec)	u_e^b	u_B^b	u_e/u_B	n_0 (cm^{-3})	v_{sh} (km s^{-1})	p^c	ϵ_e (10^{-3})	ϵ_B (10^{-3})	References
G1.9+0.3	320 ^d	0.6	8.5	0.6	50	0.22	41	0.0055	0.02	14,000	0.91	0.25	45	1
Cas A	220	2300	3.3	0.77	150	290	19	15	1	5800	3.3	86	5.8	2
Kepler	175	18	5	0.71	117	3.6	12	0.30	3	4000	11	0.58	1.1	3
Tycho	215	50	2.4	0.6	240	1.1	18	0.060	0.2	2000	0.19	5.9	100	4
SN 1006	74	19	2.2	0.6	900	0.050	2.1	0.023	0.05	5000	0.29	0.17	7.4	5
RCW 86	100 ^e	49	2.5	0.6	1260	0.025	4.0	0.0063	0.5	600	0.042	0.60	96	6

NOTE—Magnetic field values from Parizot et al. (2006) except as noted. References: 1, Carlton et al. (2011); 2, Chevalier & Oishi (2003); 3, Williams et al. (2012); 4, Williams et al. (2013); 5, Winkler et al. (2014); 6, Williams et al. (2011)

^aFrom Green (2019).

^bIn units of 10^{-10} erg cm^{-3} .

^cPressure (ρv_{sh}^2) in units of 10^{-7} dyn cm^{-2} .

^dObtained from a new measurement. See text.

^eObtained from Völk et al. (2005).

in the Large Magellanic Cloud (Borkowski et al. 2006; Williams et al. 2006), and of Kepler (Williams et al. 2012). The latter study involved analysis of a complete spectral mapping of Kepler with the *Spitzer* IRS, and extraction of spectra between $7.5 \mu\text{m}$ and $38 \mu\text{m}$ at several locations. These spectra were fit with a dust-heating shock model in which post-shock grains were heated as they were advected downstream in a constant-temperature, constant-density plasma (Borkowski et al. 2006). This model provided good descriptions of observed IR spectra, allowing extraction of post-shock densities at various points in Kepler. These densities are listed in Table 3. We require ρ_0 , which we infer by dividing those values by an assumed compression ratio r_{comp} of 4, and assuming cosmic abundances (mean mass per hydrogen atom $\mu = 1.4$).

For shock velocities, we use proper motions of expansion, as measured from *Chandra* X-ray data (Katsuda et al. 2008), in 14 regions around the periphery. We then deduce magnetic-field strengths using the simple thin-rims analysis of Eq. 5, measured from the 741-ks *Chandra* image (Reynolds et al. 2007), the same image used for the second epoch of proper-motion measurements (Katsuda et al. 2008). Then the electron energy density can be extracted from intensities measured from a radio synchrotron image (5 GHz VLA; DeLaney et al. 2002) using Eq. 13.

Kepler’s SNR is an excellent target with which to attempt this determination. The very strong N-S brightness gradient at all wavelengths indicates that the shock wave is expanding into highly asymmetric material; Blair et al. (2007) find that the density to the north is 4 – 9 times that to the south (see also Williams et al. (2012)), and the shock velocities show up to a factor 3 of variation (Katsuda et al. 2008). These wide variations allow us to examine the dependence of efficiencies on several factors. Thin X-ray rims with nonthermal spectra can be seen in several locations around the periphery. Below we outline the quantitative results of our investigation.

5.2. Density measurements

The determinations of post-shock density were based on observations of Kepler with the *Spitzer* IRS instruments: both orders of the low-resolution (LL) module ($14 - 38 \mu\text{m}$), and order 1 ($7.5 - 14 \mu\text{m}$) of the short-wavelength low-resolution (SL) module. The entire remnant was mapped with the LL instrument, and selected regions with the SL module. The observations and analysis are described in Williams et al. (2012). Figure 3 illustrates the sensitivity of model spectra to gas density. Models depend weakly on both ion temperature T_i and electron temperature T_e (see Blair et al. (2007) and Williams et al. (2012) for details). Observed electron temperatures in young SNRs are typically a few keV (Reynolds et al. 2007); we assume $kT_e = 1.5$ keV, but set uncertainties by allowing a range between 1 and 2 keV.

Broadly, variations of a factor of 30 were found in density between the faint southern rim and bright north, but values were obtained at many regions around the periphery. (Averaging over larger regions reduces the contrast to the range of 4 – 9 quoted in

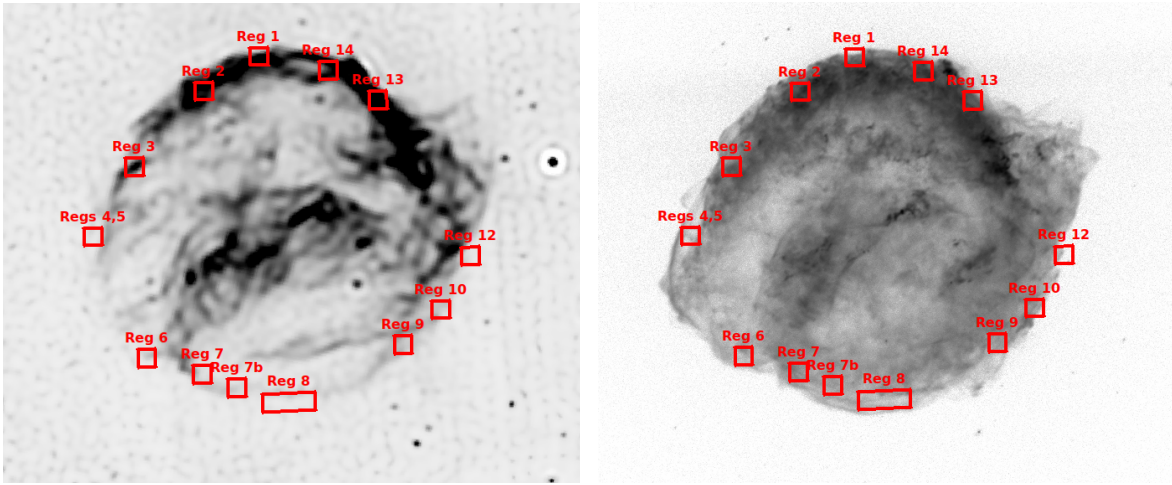


Figure 1. Left: Deconvolved *Spitzer* 24 μm image (Williams et al. 2012), with regions superposed. Right: *Chandra* image, 0.3 – 7 keV (Reynolds et al. 2007).

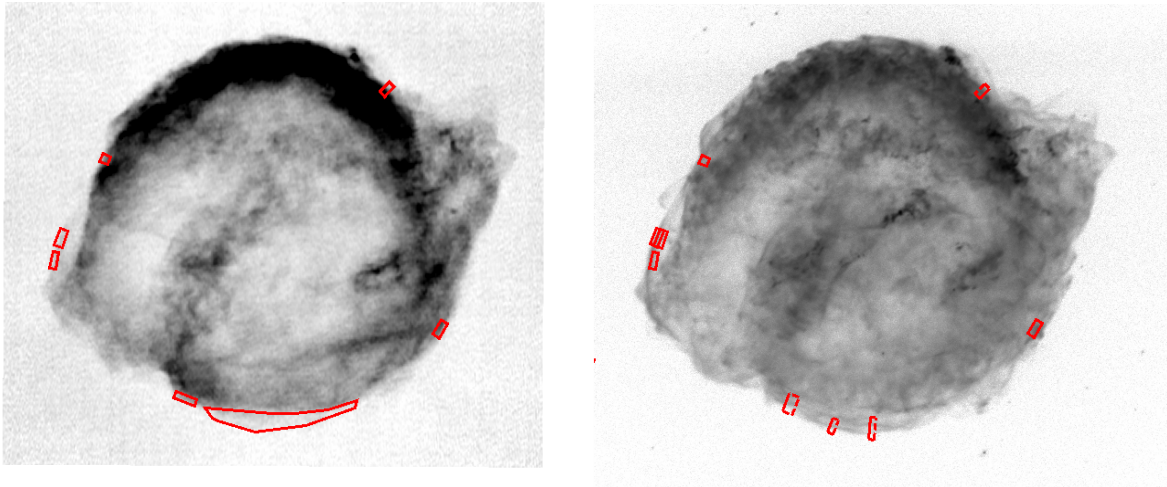


Figure 2. Left: VLA 5 GHz image (epoch 1997; DeLaney et al. 2002), showing regions used for measurements of radio intensity. These regions approximate the locations of Katsuda et al. (2008) where shock velocities were measured, and the regions of Fig. 1 where densities were obtained. Right: *Chandra* image (2006), where regions shown are where filament widths were measured. Region 4 is shown in two locations; the slightly more interior one is identical to that on the radio image to the left, but expansion between 1997 and 2006 caused the thin filament to move beyond the original region. The filament morphology did not change appreciably between 2000 and 2006, as shown in the difference image of Katsuda et al. (2008), so the slightly expanded outer region was used to measure the profile. (Reynolds et al. 2007).

Blair et al. (2007).) Figure 1 shows regions from which spectra were extracted, models fit, and densities obtained. Those densities are tabulated in Table 3. Statistical uncertainties of the fits are much smaller than the spread of values possible by changing the assumed electron temperature between 1 and 2 keV; that spread is shown in Figure 4.

While we believe the emission from each region is well-characterized by the densities listed in Table 3, in a few regions the IR emission is so faint that it is not clear if the densities listed there describe the immediate post-shock density. Fig. 1 shows that for Regions 4 and 5, 8, and 12, detectable IR is only at the innermost edge. Both Figs. 1 and 2 show the location of the blast wave as indicated by radio and nonthermal X-rays; the absence of immediate IR emission there suggests density variations along the line of sight, with IR appearing only once the density is somewhat larger (and shocks somewhat slower). For those regions, we have chosen to regard the densities of Fig. 3 as upper limits. Higher spatial-resolution IR observations, possible with JWST, will be required to improve our knowledge of the immediate post-shock density in all locations.

5.3. Shock velocities

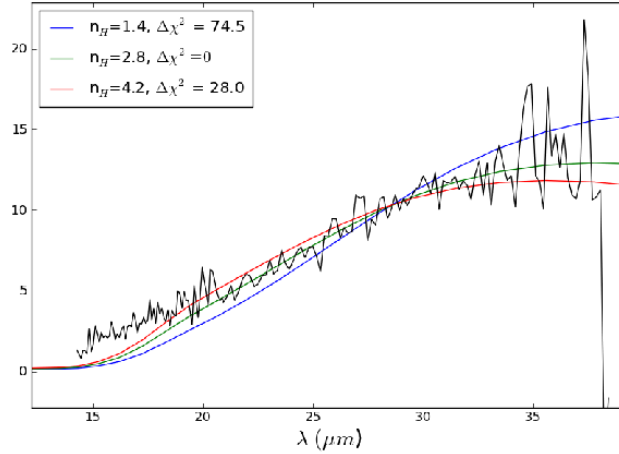


Figure 3. Region 10 observed *Spitzer* LL spectrum, with three models shown. See Williams et al. (2012) for details. The ion temperature is set by the observed shock velocity and adiabatic shock jump conditions; the electron temperature is assumed to be 1.5 keV for all regions. A least-squares algorithm is used to fit models to data, fitting between 21 and 33 μm ; shorter-wavelength emission reflects smaller grains and greater model uncertainty.

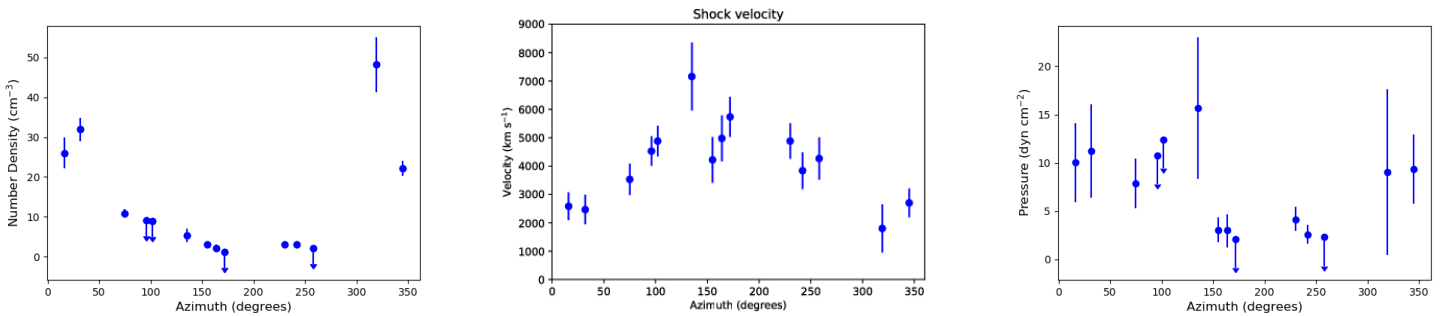


Figure 4. Observed post-shock densities (left) and shock velocities (center; Katsuda et al. 2008) at indicated positions. Uncertainties in density are given by allowing the assumed electron temperature to vary between 1 and 2 keV. Right: Pressure at different locations. Neutral upstream gas ($\mu = 1.4$) is assumed. Pressures are highest in the north, where densities are largest.

Proper motions of expansion were measured by Katsuda et al. (2008) comparing *Chandra* images obtained in 2000 and 2006, using images between 1.0 and 8.0 keV. We have converted them, and their uncertainties, into velocities for our nominal distance of 5 kpc. (Regions shown in Fig. 1 correspond to whole *Spitzer* IRS pixels. They overlap, but are not identical with, the corresponding regions used by Katsuda et al. 2008.) Figure 4 shows both densities and shock velocities of various regions. As expected, these quantities anti-correlate. Densities vary fairly smoothly around the periphery of Kepler, with lowest values in the south and highest in the north, well correlated with the brightness in radio or X-rays, while the shock velocity (with larger errors) also varies fairly smoothly in the opposite sense. Post-shock pressures $P_2 \equiv \rho v_s^2$ (again, eliding the factor $2/(\gamma - 1)$) are shown in Figure 4, where we have assumed $\rho_0 = 1.4n_H m_H/r_{\text{comp}}$, appropriate for neutral gas upstream. We take $r_{\text{comp}} = 4$.

The pressure varies by about a factor of a few around the periphery of Kepler, not unexpected given the very strong gradient in external density, with highest pressure to the north, where the external density is much larger. This magnitude of pressure variation is comparable to the radial pressure gradient in the interior of a Sedov blast wave, where the dynamical timescale is comparable to the age.

For Regions 4 and 5, 8, and 12, we regard our density determinations as upper limits, hence upper limits on the pressure. The variations in pressure we find, however, are relatively small (Fig. 4), suggesting that the true densities in those regions are unlikely to be far below those in closely neighboring regions.

5.4. Magnetic-field measurements

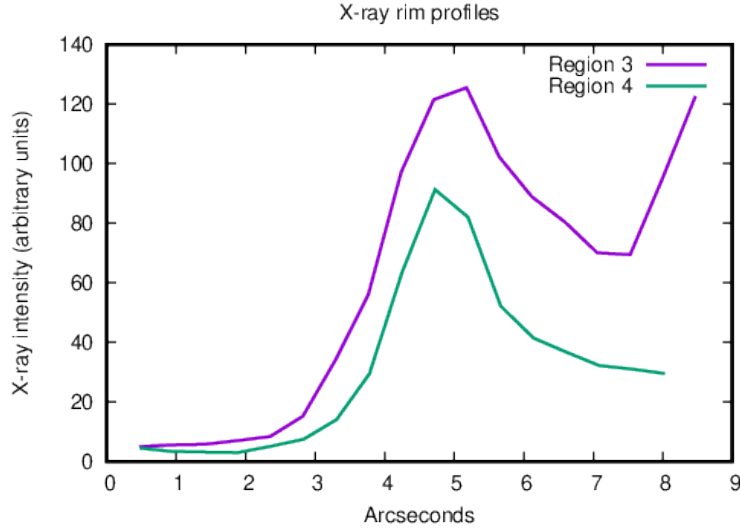


Figure 5. X-ray rim profiles of Regions 3 and 4. Measured widths are FWHMs from these figures. Estimated uncertainties are $0.2''$.

Regions shown in Fig. 2 were selected for the presence of a “thin rim” of nonthermal X-rays, from which a magnetic-field strength could be extracted, making the simplest assumptions about thin-rim physics as embodied in Equation 5. Radial profiles (averaged azimuthally over the region’s azimuthal dimensions) were extracted; two examples are shown in Fig. 5. Widths were measured at the intensity level halfway between the rim peak and the interior minimum. Uncertainties in this process were estimated to be $0.2''$, although as we shall see below, the exact value turns out not to be critical. At 5 kpc, 10^{-2} pc = $0.41''$, so for a radial width w of a rim in arcsec,

$$B = 116(v_{\text{sh}}/10^8 \text{ cm s}^{-1})^{2/3}(w'')^{-2/3} \mu\text{G}. \quad (14)$$

Note that since our shock velocities are obtained from angular proper motions, the ratio v_{sh}/w is independent of distance; we have also assumed 5 kpc to obtain the values for v_{sh} in Table 3. Values of magnetic field inferred from Eq. 14 are listed in Table 4. Not all the rim locations of Table 3 showed distinct rims, so we restrict our analysis to the seven listed in Table 4. Uncertainties are difficult to gauge, but given the large spread shown in Table 1, seem to be of order a factor of 2. The relatively narrow range of measured filament widths results in a (noisy) trend of inferred B -values with increasing shock velocity, as expected from Eq. 14.

5.5. Radio intensities

We determine mean intensities over each small region assuming it is homogeneous, and that the line-of-sight depth L is equal to the transverse extent of the filament being sampled (so generally larger than the region’s radial width). Flux densities in each region are measured from the 5 GHz radio image (DeLaney et al. 2002), then corrected for background taken from comparable or larger regions outside the remnant, divided by the solid angle $\Delta\Omega$, and extrapolated to 1 GHz assuming $j_\nu \propto \nu^{-0.71}$ everywhere. The results are listed as $\langle I_9 \rangle$ in Table 3, and the derived electron energy densities in Table 4. Quoted uncertainties result from the off-source rms fluctuation level of 0.14 mJy (DeLaney et al. 2002), scaled by the square root of the extraction area.

6. RESULTS

The globally averaged values for efficiencies for our six remnants are given in Table 2. The range is extraordinary: a factor of 500 in ϵ_e and 90 for ϵ_B . Their ratio (also equal to u_e/u_B), free of uncertainties in n_0 and less dependent on v_{sh} , ranges over a factor of 270.

However, the situation worsens when we consider spatial variations in Kepler’s remnant alone. It can easily be seen without detailed analysis that the strong north-south brightness gradient in Kepler’s radio emission requires strong spatial variations in one or both ϵ factors. Now $j_\nu \propto KB^{(s+1)/2}$ (Eq. 8) and $K \propto u_e E_l^{s-2} = \epsilon_e P_2 E_l^{s-2}$ (Eq. 7), while $B \propto (\epsilon_B P_2)^{1/2}$. This gives

$$j_\nu \propto P_2^{(s+5)/4} \epsilon_e \epsilon_B^{(s+1)/4} E_l^{-(2-s)}. \quad (15)$$

The interior of Kepler is in rough pressure equilibrium; that is, the post-shock pressure P_2 is constant within a factor of a few. Certainly E_l is constant. Then we have no way to explain the factor of 20 variation in mean intensity recorded in Table 3 other

Table 3. Observed Properties of Rim Regions

Region ^a	PA (deg)	Density n_H ^b (cm^{-3})	v_{sh} ^c (km s^{-1})	Width (arcsec)	Length (arcsec)	$\langle I_9 \rangle$ (mJy/arcsec^{-2})
1	16	26 (22, 31)	2580 ± 490			
2	32	32 (29, 39)	2470 ± 520			
3	75	11 (10, 13)	3530 ± 550	3.3	10	0.54 ± 0.06
4	96	< 9 (8, 10)	4530 ± 520	2.3	33	0.13 ± 0.04
5	102	< 9 (8, 10) ^d	4880 ± 540	2.4	33	0.17 ± 0.05
6	135	5.3 (3.6, 7.0)	7160 ± 1200			
7	155	3.0 (2.6, 3.6)	4220 ± 810	4.0	17	0.35 ± 0.04
7b ^e	164	2.1 (1.1, 3.1)	4980 ± 810			
8	172	< 1.0 (0.6, 1.4)	5740 ± 700	3.2	28	0.13 ± 0.01
9	230	3.0 (2.5, 3.5)	4880 ± 630			
10	242	3.0 (2.6, 3.6)	3840 ± 650	5.4	15	0.53 ± 0.04
12	258	< 2.0 (1.5, 2.5)	4270 ± 740			
13	319	48 (41, 62)	1800 ± 850	3.9	15	1.1 ± 0.03
14	345	22 (20, 26)	2700 ± 500			

^aNumbering in Katsuda et al. (2008).

^bPostshock density.

^cFrom Katsuda et al. (2008), scaled to a 5 kpc distance.

^dAssumed the same as Region 4.

^eBetween K08 regions 7 and 8 (see Fig. 2).

NOTE—Values for Regions 4, 5, 8, and 12 are determinations, but upper limits for densities at the extreme edge.

Table 4. Derived Properties of Regions

Region	B (μG)	u_e ($10^{-10} \text{ erg cm}^{-3}$)	u_B ($10^{-10} \text{ erg cm}^{-3}$)	u_e/u_B	P ($10^{-7} \text{ dyn cm}^{-2}$)	ϵ_e (10^{-4})	ϵ_B (10^{-4})	$u_e/u_{B_{av}}$ ^a
3	105	53	4.36	12.2	7.9	68	56	7.1
4	157	0.74	9.84	0.076	< 11	> 0.69	> 9.1	0.20
5	161	2.44	10.3	0.24	< 12	> 2.0	> 8.3	0.68
7	121	15.9	5.8	2.75	3.1	52	19	2.7
8	148	2.54	8.7	0.29	< 2.1	> 12	> 42	0.61
10	80	55.6	2.5	22	2.6	220	9.9	4.7
13	60	189	1.4	133	9.0	210	1.6	9.7

^aAssuming the median value of $B_{av} = 121 \mu\text{G}$, and $u_{B_{av}} = 5.83 \times 10^{-10} \text{ erg cm}^{-3}$, for all regions.

than strong variations of the epsilons. Certainly the line-of-sight depth L required to obtain j_ν from $\langle I_9 \rangle$ is unlikely to vary by this much.

The quantitative results of Table 4, plotted in Fig. 6, make this point clearly. Error bars shown there are not formal uncertainties, but simply illustrate an assumed factor of 2 (100%) range. Section 7.1 discusses uncertainties in detail. But Fig. 6 shows that

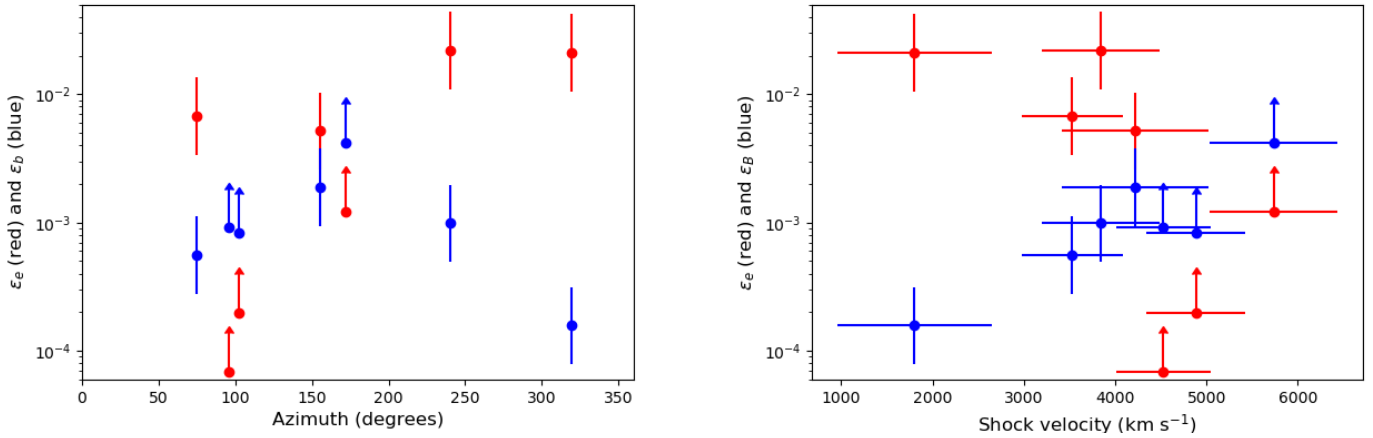


Figure 6. Left: Efficiencies of relativistic-electron acceleration ϵ_e and magnetic-field amplification ϵ_B for seven locations around the perimeter of Kepler. The values, and their ratio, scatter over orders of magnitude. Right: Efficiencies vs. shock velocity. In both cases, error bars are not formal uncertainties, but simply illustrate a range of a factor of 2. See text.

the efficiencies of magnetic-field amplification and relativistic-electron acceleration vary by a far greater amount, orders of magnitude, around the periphery of Kepler. Their ratio, completely independent of the pressure determination (and therefore of the density upper limits in some regions), varies by over three orders of magnitude, both larger and smaller than 1. Even removing the two extreme regions 4 and 13, the range is a factor of 90. In particular, adjoining regions show no particular correlation in efficiencies; the smooth trends of density or pressure with azimuth shown in Fig. 4 are not evident. Figure 6 also plots the efficiencies vs. shock velocity; while a weak trend appears to be present, it is almost entirely due to one region, 13, with a much lower shock velocity.

We also plot the dimensionless ratio u_e/u_B in Figure 7. These values also scatter widely, ranging over three orders of magnitude around Kepler's periphery, with values both larger and smaller than 1. Now the inference of u_e from observations depends strongly on the inferred magnetic-field strength (Equation 13), inducing a strong indirect dependence on shock speed through Equation 5: $u_e \propto B^{-1.71}$. Any intrinsic dependence of the observed synchrotron intensity I_ν on shock speed can be isolated by plotting the dimensionless ratio u_e/u_{Bav} , that is, using the median value of B to calculate both u_e and u_B . This quantity, Column 9 of Table 4, is plotted vs. shock speed in Figure 7. As for ϵ_B , there is the suggestion of a trend with velocity, here to lower u_e with higher shock velocity; however, the scatter is large. Figure 7 also illustrates ranges of 50% for u_e/u_B (left panel) and 30% for u_e/u_{Bav} (right panel). Since the normalization by post-shock pressure is absent, several of the uncertainties documented in Section 7.1 are not relevant for either ratio, while all variation of magnetic field is removed in the right panel. Future observational and theoretical studies should address the possibility of trends with shock velocity. Other young SNRs such as Tycho are susceptible to a spatially resolved analysis such as this.

7. DISCUSSION

Our startling results require closer examination. First, the values of ϵ_B , including the value for average remnant properties, spread over two orders of magnitude for remnant averages, and for Kepler in particular, are far lower than the 0.1 – 0.01 often assumed for nonrelativistic shocks (e.g., Lundqvist et al. 2020). A more sophisticated model for ϵ_B (Sarbadhicary et al. 2017) predicts values which, while not constant, range only over a factor of 3.

Most significant for constraining these efficiencies is the range of values around the rim of Kepler. Table 4 and Figure 6 show a particularly large range (factor of up to 300) in ϵ_e , while ϵ_B varies by a smaller, but still large factor of 35.

7.1. Possible sources of uncertainty

The magnitude of the variations among regions shown in Table 4 means that uncertainties of even factors of several cannot change the qualitative result of strong variations of efficiency. However, it is worth considering various possible sources of uncertainty.

7.1.1. Distance

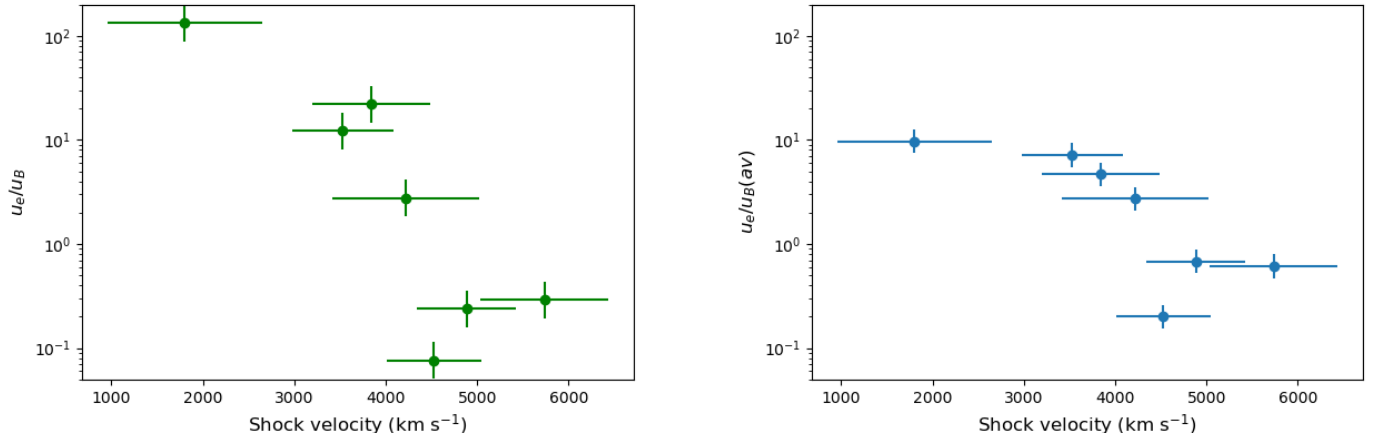


Figure 7. Left: u_e/u_B vs. shock velocity. Right: $u_e/u_{B(av)}$ vs. shock velocity (i.e., assuming the median- B value to calculate both u_e and u_B). Again, error bars are not formal uncertainties, but illustrate a range of 50% in the left panel and 30% in the right.

If shock velocities are obtained from angular proper motions, Equation 5 shows that magnetic fields inferred from the angular widths of azimuthal thin rims are independent of distance. Electron energy densities inferred from Equations 12 and 13 depend only on the distance-independent intensity I_ν and the line-of-sight depth L ; if the latter is estimated, as we do here, by the angular dimensions of the emitting region in the plane of the sky, we have $u_e \propto d^{-1}$. Alternatively since $u_e \propto j_\nu$, if an observed radio flux and angular size are used in Equation 11, we have $V_{em} \propto d^3$ so again $u_e \propto d^{-1}$. Thus $u_e/u_B \propto d^{-1}$. Our method of obtaining the density at different locations around the rim of Kepler is independent of distance, so the postshock pressure $P_2 \propto d^2$, giving $\epsilon_e \propto d^{-3}$ and $\epsilon_B \propto d^{-2}$.

The range of values of u_e in Table 2 is $\sim 10^4$, although if Cas A is removed, the range drops to 180. These values are so large compared to the factor ~ 2 which could be due to distance uncertainties, that it is hard to imagine that such uncertainties could mask or remove the dramatic trends of Table 2. The spread in values of ϵ_e and ϵ_B is considerably smaller, but ϵ_e also varies by a factor of 500 (or 51 without Cas A).

7.1.2. Density determinations

The quoted uncertainties in densities determined from fitted dust temperatures reflect primarily the range in assumed proton temperatures; the statistical errors in the fits are much smaller, for a particular model of grain composition, structure, and size distribution. The models (described in detail in Williams et al. 2011a) do make assumptions about these quantities, but they are constrained to some extent by the spectra. The most generous allowance for uncertainties in these quantities is unlikely to exceed a factor of 2 in any case.

For the regions for which we feel the true immediate post-shock density may be less than that for the emission we detect and fit in those regions (regions 4, 5, 8, and 12), there is a possibility that ϵ_e is considerably larger than the lower limits shown in Fig. 6. Since those are the lowest values, it is conceivable that the true densities could be low enough to reduce the scatter considerably. This would require, however, more than an order of magnitude difference, reducing the inferred pressure in those regions to values considerably below those in neighboring regions, well outside the scatter in pressure found elsewhere, unless blast-wave velocities are substantially lower as well. Such density variations could reflect the propagation of the blast wave into an inhomogeneous upstream medium, seen in projection. We believe it unlikely that large variations are present, but without more sensitive infrared observations at higher spatial resolution, we cannot rule out the possibility. In any case, the large scatter in ϵ_e/ϵ_B is, of course, unaffected.

7.1.3. Shock compression ratio

The compression ratio enters into the determination of the magnetic field (Equation 5) and into the upstream density as determined from collisionally heated dust downstream: $B \propto r^{-2/3}$ and $\rho_0 \propto r^{-1}$. In numerical results above, we have assumed a compression ratio of 4. We know from the presence of synchrotron rims that the blast wave in Kepler is accelerating electrons to TeV energies, and it is conceivable that the effective compression ratio is larger than 4, due either to particle escape or to an energetically significant population of relativistic ions (Jones & Ellison 1991), but it is very unlikely to be larger than the

relativistic limit of 7, since ample post-shock thermal emission indicates that the shock is not dominated by highly relativistic particles.

So $u_B \propto r^{-4/3}$ and $\epsilon_B \propto r^{-1/3}$. Then $u_e \propto B^{1+\alpha} \propto r^{-2(1+\alpha)/3}$ and $\epsilon_e \propto r^{(1-2\alpha)/3}$. For our assumed radio spectral index $\alpha = 0.71$, we have $u_e \propto r^{-1.14}$ and $\epsilon_e \propto r^{-0.14}$. For $r = 7$, then, we would reduce u_B by a factor of 0.47 and ϵ_B by 0.83, while u_e would drop by 0.53 and ϵ_e by 0.92. So at most a factor of 2 uncertainty results from this range of compression ratios.

7.1.4. Magnetic fields

As pointed out above, large uncertainties accompany the estimates of magnetic field from filament widths. However, all estimates agree on requiring substantial magnetic-field enhancement over a factor of at most 4 (or 7) increase due to shock compression alone. To estimate the effects of this uncertainty, we have assigned all regions a single value $B_{av} = 122 \mu\text{G}$, the median of the values shown in Table 4, which gives $u_B = 5.92 \times 10^{-10} \text{ erg cm}^{-3}$. The last columns of Table 4 give u_e/u_{Bav} and ϵ_{Bav} for this value of B . The spread in u_e/u_B is reduced from about 1800 to 50, which is the spread in u_e alone.

7.1.5. Radio properties

The radio spectral index of Kepler between 1.4 and 5 GHz is observed to vary with location between about 0.65 and 0.8 over most of the remnant, including all of the regions we have measured (DeLaney et al. 2002). This corresponds to a range in electron energy index s of 2.3 to 2.6. In terms of $\alpha = (s - 1)/2$, the spectral-index dependencies of the electron energy density u_e are

$$u_e \propto E_l^{1-2\alpha} (2\alpha - 1)^{-1} c_j(\alpha) B^{-(1+\alpha)} \nu^\alpha. \quad (16)$$

Evaluating this expression for the median magnetic field of $122 \mu\text{G}$, $E_l = 8.2 \times 10^{-7} \text{ erg}$, and $\nu = 1 \text{ GHz}$, for $\alpha = 0.65$ and 0.8 , gives

$$\frac{u_e(\alpha = 0.8)}{u_e(\alpha = 0.65)} = 2.4. \quad (17)$$

Very little of the scatter in the values of u_e at different locations in Kepler can be due to variations of α .

It is also unlikely that huge variations in the minimum energy of the electron distribution occur at different locations. Our fiducial value of $10m_e c^2$ simply reflects the energy at which electrons are relativistic enough for the synchrotron formulae on which our analysis rests to apply.

The radio flux measurements for the different regions carry uncertainties, as listed in Table 3. Those were obtained from the off-source rms values of 4.8 GHz radio flux in the image of DeLaney et al. (2002), scaled by the square root of the extraction area. The S/N ratio for the regions ranges from 3 for region 3 to 31 for region 13. These cannot explain the orders of magnitude spread evident in Table 4 and exhibited in Figure 6.

Finally, we obtain emissivities by assuming a line-of-sight depth of our regions, which we take to be the longer dimension of our extraction region. Again, this can easily be in error by a factor of a few, but not by orders of magnitude.

Unfortunately, we cannot calculate formal uncertainties in u_e or u_B , or their ratio. While we report uncertainties in density and shock velocity, these cannot be propagated to functions of those quantities without knowledge of their distributions, quite unlikely to be Gaussian. We know even less about the uncertainties in magnetic field. The variations among authors illustrated in Table 1 are not statistical or systematic errors, but results of applications of slightly different versions of the basic argument embodied in Equation 5. A better estimate is represented by the spread shown in Table 1 for the reference whose values we have used, Parizot et al. (2006) – of order 10%. But again, we do not know enough about the distribution of the uncertainties to be able to apply a simple error propagation formalism. Figures 6 and 7 illustrate what different levels of uncertainty would look like in the distributions; the values we have chosen represent our estimates of reasonable ranges based on the discussion above.

7.2. Consequences

We are forced to conclude that the various sources of uncertainty are dwarfed by the enormous spread of values of u_e , u_B , ϵ_e , and ϵ_B at different locations on Kepler's periphery. The primary source of the spread in u_e/u_B results from the radio brightness variations (Equation 13). We conjecture that the missing physics required to explain the spread has to do with acceleration of particles, electrons in particular, which evidently has a more complex dependence on parameters than we have included. No monotonic relation between u_e and shock velocity is apparent in the values in Tables 3 and 4; another likely possibility, the shock obliquity angle θ_{Bn} between the shock velocity and upstream magnetic field, may have a highly nonlinear effect on the ultimate population of $\sim \text{GeV}$ electrons producing the radio emission.

What has become of equipartition, the time-honored principle still often used to infer properties of synchrotron sources? First, in the SNR context, SNRs are very inefficient at producing either magnetic field energy or relativistic-particle energy. Compared,

say, to extragalactic radio sources, relatively little of the total SN energy ever winds up in nonthermal forms (that is, both epsilons are always small). It is easier to imagine wide variations in u_e/u_B when a much larger pool of thermal energy is available for any of various processes to produce electrons or magnetic field. In addition, absence of direct information on relativistic protons means that we simply have no idea what the total nonthermal energy density is (though very broad inferences from observed Galactic cosmic rays seem to require about 10% of total SN energy winding up in relativistic baryons). So electron energy densities are a small fraction of a fairly small fraction, and we should not be astonished if there is no clear relation between the energy in relativistic electrons and other pools of energy. As for magnetic energy, when SNR magnetic fields are inferred using equipartition arguments, they essentially serve as proxies for the SNR mean surface brightness Σ , as can be seen from, for instance, Pacholczyk (1970), Equation 7.14, where $B_{\text{equip}} \propto (\Sigma/D)^{2/7}$, D being the source diameter. There is no obvious mechanism which could operate to transfer energy to or from magnetic field based on the energy in relativistic electrons. Fig. 7 shows that the density-independent ratio u_e/u_B varies by orders of magnitude in regions of comparable shock velocity, emphasizing this point.

A related consequence of our results for Kepler is the problematic nature of the traditional $\Sigma - D$ relation as a diagnostic tool. The large azimuthal variations we find suggest that global averages can be very misleading. While the average values of ϵ_e and ϵ_B we obtain from the global properties for Kepler (Table 2) do fall within the large range of values at particular locations, it is not clear that those global values represent any kind of mean of the physical properties. Great care should be taken in drawing conclusions based on such global values.

One might hope to extract from this exercise some clue as to what additional parameters might be required to explain the range of efficiencies. The absence of smooth trends of efficiencies with position angle around the remnant disfavors explanations such as a smoothly varying shock obliquity angle θ_{Bn} , as one might expect for a blast wave encountering a uniform upstream magnetic field. The large scatter for adjoining regions shown in Fig. 6 requires relatively small-scale variations in properties important for particle acceleration and/or magnetic-field amplification. Our attempt to extract information relatively independent of magnetic-field inferences is shown in Fig. 7, right panel, where a noisy trend is visible as lower electron-energy density with higher shock velocity. We do not claim the unambiguous existence of such a relation since the apparent trend is strongly dependent on one or two points, but the data might offer a clue toward identifying the additional physics evidently necessary to fully understand electron acceleration in strong shock waves.

8. CONCLUSIONS

We have used a combination of radio, infrared, and X-ray data to estimate nonthermal energy densities in relativistic electrons and magnetic field first, in global averages over six young supernova remnants, and second, for seven regions around the periphery of Kepler’s supernova remnant. For the various remnants, we find enormous ranges of these quantities, with u_e/u_B varying by a factor of over 3000 (or among the Type Ia remnants, i.e., excluding Cas A, by a factor of 70). The efficiencies range from 10^{-4} to 0.05 for ϵ_e and from 0.002 to 0.1 for u_B . There are no clear trends with age or shock speed evident in Table 2.

Of course, the collection of remnants is quite inhomogeneous, and the objects themselves are inhomogeneous, so describing them by global average values may conceal systematic trends in these quantities. We have therefore extracted densities, shock speeds, magnetic-field strengths, and radio fluxes from seven regions around Kepler, and find similarly large spreads in the energy densities, their ratio, and the efficiencies. Figures 6 and 7 summarize the results.

The variations in our inferred values are so large that even conservative assessments of sources of error or uncertainty are quite unable to account for them. There seems no alternative but to conclude that additional parameters must influence the amplification of magnetic field and acceleration of electrons. Various possibilities come to mind: the neutral fraction of upstream gas, the obliquity angle between the local shock normal and the upstream magnetic-field direction, or downstream variations in, for instance, magnetic turbulence. Evidence for local variations of shock-acceleration physics at different points around SNR peripheries (through the dimensionless diffusion coefficient $\eta \equiv \lambda_{\text{mfp}}/r_L$, the ratio of mean free path to Larmor radius) has recently been presented by Tsuji et al. (2021); the origins of the variations of η they find presumably rely on some of these additional parameters.

Given our evident lack of understanding of all the factors that contribute to shock acceleration of particles and turbulent amplification of magnetic field, it would seem that assumptions of, for instance, constant values of the efficiency as a function of time or local conditions in synchrotron sources should be made with extreme caution, and borne in mind as possible sources of systematic error or completely incorrect inference when analyzing spectra of such objects as gamma-ray bursters or radio supernovae.

This work was supported by NASA grants NNX11AB14G through the ADAP program and award RSA 1378040 through the *Spitzer* program. We thank Tracey De Laney for making available the Kepler radio data. A preliminary version of this work was presented in Reynolds et al. (2012b).

REFERENCES

- Bamba, A., Yamazaki, R., Ueno, M., & Koyama, K. 2003, *ApJ*, 589, 827, doi: [10.1086/374687](https://doi.org/10.1086/374687)
- Bartel, N., Bietenholz, M. F., Rupen, M. P., et al. 1994, *Nature*, 368, 610, doi: [10.1038/368610a0](https://doi.org/10.1038/368610a0)
- Blair, W. P., Ghavamian, P., Long, K. S., et al. 2007, *ApJ*, 662, 998, doi: [10.1086/518414](https://doi.org/10.1086/518414)
- Blandford, R., & Eichler, D. 1987, *Phys.Rep.*, 154, 1, doi: [10.1016/0370-1573\(87\)90134-7](https://doi.org/10.1016/0370-1573(87)90134-7)
- Borkowski, K. J., Reynolds, S. P., Hwang, U., et al. 2013, *ApJL*, 771, L9, doi: [10.1088/2041-8205/771/1/L9](https://doi.org/10.1088/2041-8205/771/1/L9)
- Borkowski, K. J., Williams, B. J., Reynolds, S. P., et al. 2006, *ApJL*, 642, L141, doi: [10.1086/504472](https://doi.org/10.1086/504472)
- Burbidge, G. R. 1956, *ApJ*, 124, 416, doi: [10.1086/146237](https://doi.org/10.1086/146237)
- Carlton, A. K., Borkowski, K. J., Reynolds, S. P., et al. 2011, *ApJL*, 737, L22, doi: [10.1088/2041-8205/737/1/L22](https://doi.org/10.1088/2041-8205/737/1/L22)
- Chevalier, R. A. 1984, *Annals of the New York Academy of Sciences*, 422, 215, doi: [10.1111/j.1749-6632.1984.tb23355.x](https://doi.org/10.1111/j.1749-6632.1984.tb23355.x)
- . 1998, *ApJ*, 499, 810, doi: [10.1086/305676](https://doi.org/10.1086/305676)
- Chevalier, R. A., & Oishi, J. 2003, *ApJL*, 593, L23, doi: [10.1086/377572](https://doi.org/10.1086/377572)
- Chomiuk, L., & Wilcots, E. M. 2009, *ApJ*, 703, 370, doi: [10.1088/0004-637X/703/1/370](https://doi.org/10.1088/0004-637X/703/1/370)
- Crumley, P., Caprioli, D., Markoff, S., & Spitkovsky, A. 2019, *MNRAS*, 485, 5105, doi: [10.1093/mnras/stz232](https://doi.org/10.1093/mnras/stz232)
- DeLaney, T., Koralesky, B., Rudnick, L., & Dickel, J. R. 2002, *ApJ*, 580, 914, doi: [10.1086/343787](https://doi.org/10.1086/343787)
- Dwek, E., & Arendt, R. G. 1992, *ARAA*, 30, 11, doi: [10.1146/annurev.aa.30.090192.000303](https://doi.org/10.1146/annurev.aa.30.090192.000303)
- Fransson, C., & Björnsson, C.-I. 1998, *ApJ*, 509, 861, doi: [10.1086/306531](https://doi.org/10.1086/306531)
- Green, D. A. 2019, *Journal of Astrophysics and Astronomy*, 40, 36, doi: [10.1007/s12036-019-9601-6](https://doi.org/10.1007/s12036-019-9601-6)
- Jones, F. C., & Ellison, D. C. 1991, *SSR*, 58, 259, doi: [10.1007/BF01206003](https://doi.org/10.1007/BF01206003)
- Katsuda, S., Tsunemi, H., Uchida, H., & Kimura, M. 2008, *ApJ*, 689, 225, doi: [10.1086/592376](https://doi.org/10.1086/592376)
- Lundqvist, P., Kundu, E., Pérez-Torres, M. A., et al. 2020, *ApJ*, 890, 159, doi: [10.3847/1538-4357/ab6dc6](https://doi.org/10.3847/1538-4357/ab6dc6)
- Malkov, M. A., & Drury, L. O. 2001, *RPP*, 64, 429, doi: [10.1088/0034-4885/64/4/201](https://doi.org/10.1088/0034-4885/64/4/201)
- Millard, M. J., Bhalerao, J., Park, S., et al. 2019, arXiv e-prints, arXiv:1905.04475. <https://arxiv.org/abs/1905.04475>
- Nava, L., Vianello, G., Omodei, N., et al. 2014, *MNRAS*, 443, 3578, doi: [10.1093/mnras/stu1451](https://doi.org/10.1093/mnras/stu1451)
- Pacholczyk, A. G. 1970, *Radio astrophysics. Nonthermal processes in galactic and extragalactic sources* (San Francisco: Freeman)
- Panaiteanu, A., & Kumar, P. 2001, *ApJL*, 560, L49, doi: [10.1086/324061](https://doi.org/10.1086/324061)
- Parizot, E., Marcowith, A., Ballet, J., & Gallant, Y. A. 2006, *A&A*, 453, 387, doi: [10.1051/0004-6361:20064985](https://doi.org/10.1051/0004-6361:20064985)
- Pavlović, M. Z., Urošević, D., Arbutina, B., et al. 2018, *ApJ*, 852, 84, doi: [10.3847/1538-4357/aaa1e6](https://doi.org/10.3847/1538-4357/aaa1e6)
- Pohl, M., Yan, H., & Lazarian, A. 2005, *ApJL*, 626, L101, doi: [10.1086/431902](https://doi.org/10.1086/431902)
- Ressler, S. M., Katsuda, S., Reynolds, S. P., et al. 2014, *ApJ*, 790, 85, doi: [10.1088/0004-637X/790/2/85](https://doi.org/10.1088/0004-637X/790/2/85)
- Rettig, R., & Pohl, M. 2012, *A&A*, 545, A47, doi: [10.1051/0004-6361/201219409](https://doi.org/10.1051/0004-6361/201219409)
- Reynolds, S. P., Borkowski, K. J., Green, D. A., et al. 2008, *ApJL*, 680, L41, doi: [10.1086/589570](https://doi.org/10.1086/589570)
- Reynolds, S. P., Borkowski, K. J., Hwang, U., et al. 2007, *ApJL*, 668, L135, doi: [10.1086/522830](https://doi.org/10.1086/522830)
- Reynolds, S. P., & Chevalier, R. A. 1981, *ApJ*, 245, 912, doi: [10.1086/158868](https://doi.org/10.1086/158868)
- Reynolds, S. P., Gaensler, B. M., & Bocchino, F. 2012a, *SSR*, 166, 231, doi: [10.1007/s11214-011-9775-y](https://doi.org/10.1007/s11214-011-9775-y)
- Reynolds, S. P., Williams, B., Borkowski, K., et al. 2012b, in *American Astronomical Society Meeting Abstracts*, Vol. 219, American Astronomical Society Meeting Abstracts #219, 239-20
- Riquelme, M. A., & Spitkovsky, A. 2011, *ApJ*, 733, 63, doi: [10.1088/0004-637X/733/1/63](https://doi.org/10.1088/0004-637X/733/1/63)
- Sankrit, R., Blair, W. P., Delaney, T., et al. 2005, *AdSpRes*, 35, 1027, doi: [10.1016/j.asr.2004.11.018](https://doi.org/10.1016/j.asr.2004.11.018)
- Sankrit, R., Raymond, J. C., Blair, W. P., et al. 2016, *ApJ*, 817, 36, doi: [10.3847/0004-637X/817/1/36](https://doi.org/10.3847/0004-637X/817/1/36)
- Sarbadhicary, S. K., Badenes, C., Chomiuk, L., Caprioli, D., & Huizenga, D. 2017, *MNRAS*, 464, 2326, doi: [10.1093/mnras/stw2566](https://doi.org/10.1093/mnras/stw2566)
- Sari, R., Piran, T., & Narayan, R. 1998, *ApJL*, 497, L17, doi: [10.1086/311269](https://doi.org/10.1086/311269)
- Tran, A., Williams, B. J., Petre, R., Ressler, S. M., & Reynolds, S. P. 2015, *ApJ*, 812, 101, doi: [10.1088/0004-637X/812/2/101](https://doi.org/10.1088/0004-637X/812/2/101)
- Tsuji, N., Uchiyama, Y., Khangulyan, D., & Aharonian, F. 2021, *ApJ*, 907, 117, doi: [10.3847/1538-4357/abce65](https://doi.org/10.3847/1538-4357/abce65)
- van Paradijs, J., Kouveliotou, C., & Wijers, R. A. M. J. 2000, *ARA&A*, 38, 379, doi: [10.1146/annurev.astro.38.1.379](https://doi.org/10.1146/annurev.astro.38.1.379)
- Vink, J., & Laming, J. M. 2003, *ApJ*, 584, 758, doi: [10.1086/345832](https://doi.org/10.1086/345832)

- Völk, H. J., Berezhko, E. G., & Ksenofontov, L. T. 2005, *A&A*, 433, 229, doi: [10.1051/0004-6361:20042015](https://doi.org/10.1051/0004-6361:20042015)
- Weiler, K. W., Panagia, N., Montes, M. J., & Sramek, R. A. 2002, *ARA&A*, 40, 387, doi: [10.1146/annurev.astro.40.060401.093744](https://doi.org/10.1146/annurev.astro.40.060401.093744)
- Williams, B. J., Borkowski, K. J., Ghavamian, P., et al. 2013, *ApJ*, 770, 129, doi: [10.1088/0004-637X/770/2/129](https://doi.org/10.1088/0004-637X/770/2/129)
- Williams, B. J., Borkowski, K. J., Reynolds, S. P., et al. 2012, *ApJ*, 755, 3, doi: [10.1088/0004-637X/755/1/3](https://doi.org/10.1088/0004-637X/755/1/3)
- . 2006, *ApJL*, 652, L33, doi: [10.1086/509876](https://doi.org/10.1086/509876)
- Williams, B. J., Blair, W. P., Blondin, J. M., et al. 2011, *ApJ*, 741, 96, doi: [10.1088/0004-637X/741/2/96](https://doi.org/10.1088/0004-637X/741/2/96)
- Winkler, P. F., Williams, B. J., Reynolds, S. P., et al. 2014, *ApJ*, 781, 65, doi: [10.1088/0004-637X/781/2/65](https://doi.org/10.1088/0004-637X/781/2/65)